mater.scichina.com link.springer.com https://doi.org/10.1007/s40843-025-3545-7

SPECIAL ISSUE: 2026 Emerging Investigator Issue

Magnetic oxygen-generating robots via a self-healing hydrogel-based modular assembly strategy

Jingjing Qin[1†], Jiahao Li[2†], Kaibin Chu[1], Haoxiang Chen[3], Pengyang Xuan[1], Xiuming Wu[1], Hongliang Dong[4,7], Xiaoyuan Peng[5], Yun Qian[5], Silvio Osella[6], Yujie Chen[3], Wei Fan[1], Tianxi Liu[1] and Feili Lai[3,8*]

ABSTRACT **Magnetically driven hydrogel robots exhibit significant potential in biomedical and underwater applications owing to their remote controllability, flexibility, biocompatibility, and chemical stability. However, the lack of functional integration in existing hydrogel robots limits their adaptability to diverse applications. In this work, a novel universal strategy for modular assembly of hydrogels has been introduced, which involves the incorporation of magnetic particles within a self-healing κ-carrageenan/polyacrylamide-based hydrogel, facilitating the free assembly of magnetic actuation modules. These modules can construct magnetic soft robots characterized by complex geometries and magnetization distributions, allowing for diverse deformations under magnetic fields. Furthermore, this strategy enables the integration of additional functionalities, such as photocatalysis. The free assembly of functional modules embedded with specifically designed photocatalysts (e.g., Ru-Bi_2CrO_6) and magnetic actuation modules results in an oxygen-generating robot. The robot demonstrates flexible underwater movement through magnetically controlled oscillatory actuation, effectively reducing water agitation while providing a stable oxygen supply to specific aquatic environments via photocatalytic oxygen generation, achieving an oxygen evolution rate of 389.1 μmol g^{-1} h^{-1}. The hydrogel skeleton of the oxygen-generating robot effectively suppresses photocatalytic particle aggregation and sedimentation, while enabling facile magnetic recovery. This innovative method provides a scalable and adaptable approach to the design and multifunctional integration of soft robots.**

Keywords: smart material, magnetic soft robot, photocatalytic oxygen generation, self-healing

INTRODUCTION

In recent years, soft robots have demonstrated remarkable potential in biomedical applications and aquatic environmental remediation due to their exceptional environmental adaptability and safe human-machine interaction capabilities [1–4]. Particularly, magnetically actuated robots have emerged as a pivotal approach for developing soft robotic systems capable of complex motions and morphological transformations, owing to their unique advantages in remote maneuverability, fuel-free operation, programmability, and recyclability [5–7]. A variety of magnetically responsive smart materials, including hydrogel composites and elastomers, have been developed to enable diverse motile behaviors such as crawling and folding [8,9]. Among them, magnetically actuated hydrogel robots, which comprise hydrogels embedded with magnetic particles, have garnered significant attention in constructing flexible underwater robotic systems by synergistically integrating magnetic responsiveness with the inherent advantages of hydrogels, including flexibility, biocompatibility, and chemical stability [10–12]. However, current research primarily focuses on the actuation of soft robots, lacking functional integration, thereby limiting their expansion into diversified application scenarios.

As exemplified by addressing the imbalance in dissolved oxygen dynamics in specific water bodies, such as aquariums or localized water areas, photocatalytic oxygen generation technology demonstrates green and sustainable potential in ecological restoration [13–15]. In recent years, bismuth-based materials have garnered substantial attention from researchers in

[1] The Key Laboratory of Synthetic and Biological Colloids, Ministry of Education, School of Chemical and Material Engineering, International Joint Research Laboratory for Nano Energy Composites, Jiangnan University, Wuxi 214122, China
[2] CAS Key Laboratory of Mechanical Behavior and Design of Materials, Department of Modern Mechanics, CAS Center for Excellence in Complex System Mechanics, University of Science and Technology of China, Hefei 230027, China
[3] State Key Laboratory of Metal Matrix Composites, School of Materials Science and Engineering, Shanghai Jiao Tong University, Shanghai 200240, China
[4] Center for High Pressure Science and Technology Advanced Research, Shanghai 201203, China
[5] Department of Orthopaedics, Shanghai Sixth People's Hospital Affiliated to Shanghai Jiao Tong University School of Medicine, Shanghai 200233, China
[6] Chemical and Biological Systems Simulation Lab, Centre of New Technologies, University of Warsaw, Warsaw 02-097, Poland
[7] Shanghai Key Laboratory of Material Frontiers Research in Extreme Environments (MFree), Shanghai Advanced Research in Physical Sciences (SHARPS), Shanghai 201203, China
[8] Department of Chemistry, KU Leuven, Celestijnenlaan 200F, Leuven 3001, Belgium
† Equally contributed to this work.
* Corresponding author (email: feililai@sjtu.edu.cn or feili.lai@kuleuven.be)

the field of photocatalysis, exhibiting remarkable potential as photocatalysts. From the perspective of atomic orbital structure, the specific orbital configuration of Bi^{3+} (e.g., the occupancy state of its 6s/5d orbitals) plays a pivotal role in regulating the energy level distribution and structural construction of the material's bands [16]. This distinctive electronic structure serves as a theoretical foundation and offers practical feasibility for the precise modulation of the materials' band structures and electronic properties [17]. Bismuth chromates, an essential subset within the bismuth-based material family, manifest diverse chemical compositions and crystal structures, primarily attributed to the variable oxidation states of chromium. By precisely tuning parameters such as crystal structure, the directional optimization of the physical and chemical properties of these materials can be accomplished. This characteristic confers upon them significant exploratory value and promising application prospects in frontier research areas, such as photocatalysis. Tao *et al.* developed the Bi_2CrO_6 in triclinic crystalline phase, which exhibited a broad light absorption range (<650 nm) and high charge carrier mobility, providing insights for photocatalytic water splitting toward oxygen generation [18]. Nevertheless, the relatively intrinsic surface reaction inertness of this material critically compromises its practical catalytic activity. Elemental doping strategies currently stand as one of the most effective approaches to address this fundamental limitation [19,20]. Especially, owing to the superior chemical stability and high catalytic activity of Ru [21,22], the Ru doping strategy is anticipated to enhance the photocatalytic performance of Bi_2CrO_6 in oxygen generation by modulating its electron cloud distribution, improving visible-light absorption, and establishing a built-in electric field conducive to photogenerated charge carrier separation. Notably, photocatalytic technologies face inherent limitations in practical applications, including catalyst agglomeration and deactivation as well as the necessity of mechanical agitation to maintain suspension [23,24], while conventional agitation methods risk compromising aquatic ecological balance. Moreover, existing photocatalytic approaches lack operational flexibility in precisely controlling treatment locations within aquatic environments, while the recovery of photocatalytic particles remains challenging. Consequently, there is a critical need to develop novel magnetically actuated hydrogel robots capable of programmable locomotion and integrated photocatalytic functionality in underwater settings. The three-dimensional (3D) porous framework of hydrogel robots serves as an effective carrier for photocatalysts, preventing particle aggregation and enabling efficient recovery. Simultaneously, the flexible and controllable deformation of robots can generate partial hydrodynamic disturbance to enhance the mass transfer rate of catalytic reactions, thereby achieving water oxygenation. Nevertheless, the development of strategies synergistically integrating programmable magnetic actuation with high-efficiency photocatalytic oxygen generation capabilities remains a critical challenge.

Currently, a desirable strategy for fabricating magnetically driven soft robots with programmable motion involves creating magnetic materials possessing complex geometries and magnetization distributions [25]. Various advanced fabrication techniques, including additive manufacturing, have been developed, which enable the creation of intricate shapes and magnetization distributions via physical alignment of magnetic dipoles and curing of the matrix [26,27]. For example, Kim *et al.* utilized a direct ink writing technique to manipulate complex magnetization patterns in 3D printed magnetically responsive materials to achieve a predetermined shape deformation [27]. However, the magnetization of the above methods is coupled with the manufacturing process, which prevents changes to the geometry and magnetization distribution after fabrication, as well as making it difficult to integrate other functionalities (e.g., oxygen enrichment in water bodies). It also remains challenging to construct 3D structures of magnetic composites with complex shapes through the direct 3D printing technique. In terms of more convenient preparation of magnetically driven materials, methods for assembling and magnetization programming of magnetic material modules have been proposed to effectively combine them into larger and more complex two-dimensional (2D) structures [28]. Nevertheless, most of the existing magnetic assemblies are based on physical connections of different magnetic modules to each other, which can be easily damaged under external perturbations.

Hydrogels with self-healing capabilities provide an ideal platform for module assembly. Due to the adjustable structures and diverse functionalities of hydrogels, their self-healing properties can be achieved by introducing reversible physical or chemical bonds [29–34]. It has been investigated that κ-carrageenan (KC) exhibits cation sensitivity (e.g., K^+ ions) and thermally reversible phase transitions, which exhibits double helices in structure at low temperature and dissociates into single chains at high temperature [35–37]. Therefore, the double-network hydrogels prepared containing KC may have excellent self-healing ability, as well as improved mechanical properties.

In this work, a method for assembling magnetic soft robots utilizing the self-healing properties of hydrogels is proposed, enabling programmable deformation and the integration of functionalities. Incorporating hard magnetic microparticles into KC/polyacrylamide (KC/PAm) dual-network hydrogels results in the creation of a series of magnetic actuation modules that possess self-healing properties to enable flexible assembly into soft robots with complex geometries and magnetization distributions. Under magnetic field actuation, these soft robots demonstrate multiple shape transformation modes for various potential applications (e.g., photocatalytic oxygen generation). By integrating a well-designed Ru-doped Bi_2CrO_6 (Ru-Bi_2CrO_6, as an example) photocatalyst into the KC/PAm dual network, a functional oxygen-evolving module has been successfully constructed. This module can be further assembled with a magnetic driving module to form a magnetic oxygen-generating robot (OGR), enabling targeted oxygen supply in aquatic environments. This study provides new approaches for the development of programmable soft robots and the construction of functionally integrated soft robotic systems. Simultaneously, it offers new insights into the design of efficient oxygen-evolving photocatalytic systems.

EXPERIMENTAL SECTION

Materials

Ruthenium chloride ($RuCl_3$), KC, and 3-(trimethoxysilyl) propyl methacrylate (TMSPMA) were purchased from Shanghai Adamasi Reagents Co., Ltd. Acrylamide (Am), potassium chloride (KCl), bismuth nitrate pentahydrate ($Bi(NO_3)_3{\cdot}5H_2O$), nitric acid (HNO_3), potassium chromate (K_2CrO_4), ammonium persulfate (APS), aqueous ammonia ($NH_3{\cdot}H_2O$), silver nitrate

($AgNO_3$), ethylene glycol (EG), acetone, and ethanol were purchased from Sinopharm Chemical Reagent Co., Ltd. *N,N'*-methylenebis(acrylamide) (MBA) was purchased from Shanghai Macklin Biochemical Technology Co., Ltd. NdFeB microparticle was purchased from Guangzhou Xinnuode Transmission Part Co., Ltd.

Preparation of TMSPMA-modified NdFeB (T-NdFeB)

In a triple-neck flask, 5 g of NdFeB powder, 238 mL of ethanol, and 12 mL of TMSPMA were added sequentially, and stirred under an ice bath for 24 h. The obtained T-NdFeB was then washed with deionized water three times and dried at 60 °C.

Preparation of T-NdFeB/KC/PAm (T-NKP) hydrogel

In a triple-necked flask, 0.4 g of KC was dissolved completely into 15 mL of deionized water by stirring at 80 °C for 2 h. After the temperature of the above solution was reduced to 60 °C, 1.5 g of T-NdFeB was added and stirred for 30 min. Then, 3.2 g of Am, 1.6 mg of MBA, 24 mg of KCl, and 32 mg of APS were also dissolved, which was transferred to a mold, polymerized at 60 °C for 5 h, and followed by a placement in an environment at 4 °C for 1 h. The hydrogel obtained is noted as T-NKP-1.5, where "1.5" represents the added T-NdFeB mass (1.5 g in this sample). The hydrogel prepared from NdFeB without modification by TMSPMA was marked as NKP hydrogel.

Preparation of magnetic actuation module

The magnetic actuation module was obtained by magnetizing T-NKP-1.5 hydrogel with a suitable size and shape using a magnetizing apparatus (SFY-2070, Shenzhen Shengfengyuan Automation Equipment Co., Ltd.).

Preparation of Bi_2CrO_6

Bi_2CrO_6 was synthesized by a hydrothermal method. In a typical procedure, 2 mmol of $Bi(NO_3)_3{\cdot}5H_2O$ and 1 mmol of K_2CrO_4 were dissolved in 30 mL of 2 M HNO_3 solution. The pH of the above solution was adjusted to 1.0 with $NH_3{\cdot}H_2O$ under vigorous stirring. The obtained yellow precursor was then transferred to a Teflon-lined stainless-steel autoclave and hydrothermally treated at 180 °C for 10 h. After cooling to room temperature, a red precipitate was obtained, washed with deionized water, and dried at 60 °C.

Preparation of Ru-Bi_2CrO_6

Bi_2CrO_6 (0.0995 g) was dispersed in 30 mL of EG, followed by the addition of 1 mg of $RuCl_3$. The resulting dispersion was stirred at 180 °C for 10 h, which was subsequently filtered and dried to obtain the sample. The obtained sample was heated to 350 °C in a muffle furnace and maintained for 3 h to obtain Ru-Bi_2CrO_6.

Preparation of functional module

The preparation of the functional module was similar to that of T-NKP-1.5 hydrogel, except that 1.5 g of T-NdFeB was replaced by 0.5 g of Ru-Bi_2CrO_6. The obtained Ru-Bi_2CrO_6/KC/PAm hydrogel was used as a functional module.

Assembly of modules

The cut surfaces of the two hydrogels were contacted together, which were sealed in a polyethylene bag and immersed in a water bath at 80 °C for 1 h. Subsequently, they were placed at 4 °C for 30 min to obtain the healed sample. The magnetic actuation module could be assembled into a complete unit after the above self-healing process to obtain a magnetic soft robot. The soft robot assembled with magnetic actuation and functional modules was noted as OGR.

The healing efficiency was evaluated by comparing the tensile strengths of pristine and self-healed hydrogels, and defined as:

$$\text{Healing efficiency} = \sigma_1/\sigma_0 \times 100\%,$$

where σ_0 and σ_1 represent the tensile strengths of the original and self-healed hydrogels, respectively.

Photocatalytic performance for oxygen generation

0.05 g of photocatalyst (or OGR) was dispersed into 100 mL of solution containing 3 mM $AgNO_3$. The vessel was sealed and filled with Ar to drive out the air before the test. The photocatalytic system was irradiated vertically for 3 h using a 300 W xenon lamp positioned 10 cm from the reaction solution. The reaction temperature was maintained at 20 °C through a circulating water bath. The generated oxygen was detected by gas chromatography (GC, GC9790plus, Ar carrier, Zhejiang Fuli Analytic Instruments Co., Ltd.). For the photocatalytic processes of Bi_2CrO_6 and Ru-Bi_2CrO_6 powders, continuous stirring was required to ensure their homogeneous dispersions.

Magnetically driven process

Motion control of the soft robot was achieved through the coordinated action of a 3D magnetic field. Specifically, an alternating square-wave magnetic field (18 mT, 3 Hz) was applied along the *Z*-axis to induce periodic oscillatory motion at the tail of OGR, thereby providing the primary driving force. Meanwhile, a static magnetic field of 15 mT was superimposed along the *X*- or *Y*-axis, enabling precise steering control by real-time modulation of the magnetic field direction within the horizontal plane.

Measurement of dissolved oxygen (DO) concentrations around OGR in simulated hypoxic water environment

Firstly, the temperature was maintained at 20 °C and the container was filled with deionized water. Then, Ar gas was continuously bubbled into the container for 30 min to simulate a hypoxic water environment. Next, five OGRs were placed in the simulated hypoxic water environment and then irradiated with a 300 W xenon lamp. The photocatalytic oxygen-generating reaction was confined to a localized area. After 6 h of illumination, the DO concentrations in the water were measured at multiple positions around the OGR, including near the OGR and at varying distances.

RESULTS AND DISCUSSION

As shown in Fig. 1a, a programmable magnetic soft robot, consisting of functionalized hard magnetic microparticles (NdFeB) and reversibly cross-linked hydrogel matrix, was wisely designed. As a proof of concept, by combining an ionically cross-linked KC network with a covalent polyacrylamide (PAm) network, KC/PAm composite hydrogel with double cross-linked networks was selected for preparation. The NdFeB microparticles were treated by TMSPMA, which introduces C=C groups on TMSPMA to the surface of NdFeB microparticles (Fig. S1). Furthermore, T-NKP hydrogels were obtained by incorporating T-NdFeB microparticles into the precursor solu-

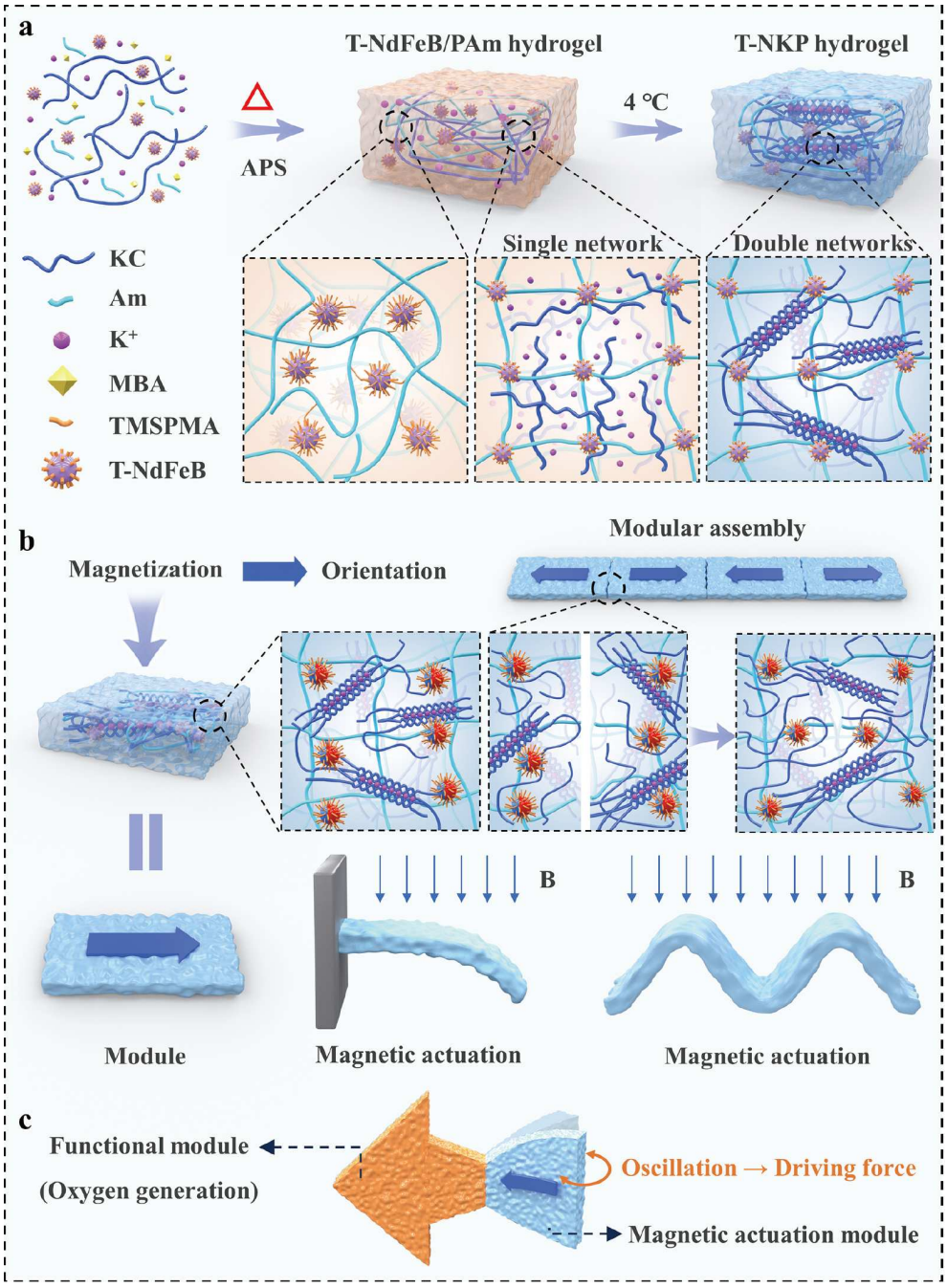

Figure 1 Schematic illustrations for (a) the preparation of T-NKP and (b) assembling magnetic soft robots. (c) Assembly and driving mechanism of the OGR.

tion of KC/PAm hydrogel, followed by polymerization. The C=C groups on the T-NdFeB microparticles are capable of participating in free radical polymerization with C=C bonds in PAm and MBA, resulting in enhanced stability and distribution of NdFeB microparticles in the hydrogel (Fig. S2). The T-NKP hydrogel was selected as a modular unit and constructed into a larger structure through magnetization and assembly processes (Fig. 1b). Based on the aforementioned principle, it is also feasible to integrate additional functionalities (e.g., photocatalytic oxygen generation) by combining magnetic and functional modules (Fig. 1c), leading to the successful fabrication of OGR.

Fourier transform infrared spectroscopy (FT-IR) was employed to analyze the chemical structure of T-NKP, as depicted in Fig. S3. The prominent peak observed at 3434 cm^{-1} corresponds to the –OH group and N–H bond stretching of the amide group, while the peak at 1658 cm^{-1} is attributed to the carbonyl group within the Am moiety [38]. To be noted, a distinct peak at 1089 cm^{-1} indicative of Si–O bond emerges in the FT-IR spectrum of T-NKP, confirming the successful functionalization of NdFeB microparticles with TMSPMA molecules [39,40]. The morphologies of various hydrogels were observed by scanning electron microscopy (SEM) technique. As shown in Fig. S4a, the PAm hydrogel is porous with an average pore diameter of 40 μm, which is slightly larger than that of KC/PAm

hydrogel (10 μm) with dense pore wall (Fig. S4b). After the addition of magnetic T-NdFeB microparticles, the T-NKP hydrogel is maintained porous with a pore diameter of approximately 40 μm and uniform distributions of T-NdFeB microparticles on the pore walls of the hydrogel (Fig. S5). The energy dispersive spectroscopy (EDS) elemental mappings of the T-NKP hydrogel indicate that C, N, O, S, Nd, Fe, B, and Si elements are uniformly distributed throughout the hydrogel, which further prove the successful preparation of T-NKP hydrogel.

The self-healing abilities of NKP and T-NKP hydrogels are discussed in Fig. 2. A rectangular hydrogel was cut into two pieces, which were re-contacted and maintained in an environment at 80 °C for 1 h. Then, the above integrated piece was transferred to an environment at 4 °C for a short holding time of 20 min. After the above steps, the self-healing hydrogel could withstand a certain degree of stretching (approximately 59%) deformation without breaking apart (Fig. 2a). As the schematic illustration for the self-healing process of the T-NKP shown in Fig. 2b, the double helix-shaped KC is able to transform into coils during the heating process, leading to the self-healing property of T-NKP hydrogel. The toughness of T-NKP hydrogel is determined not only by the KC/PAm double networks but also by the T-NdFeB microparticles. By comparing three kinds of hydrogels with different T-NdFeB contents, it is observed that the elongation decreases from 832.7% to 25.0% with the increase of added T-NdFeB content from 0 to 2 g, but the Young's modulus exhibits a significant increase (Fig. 2c). Based on the stress-strain curves of T-NKP-1.5 and NKP-1.5 hydrogels, their enhanced mechanical properties originate from the incorporation of T-NdFeB microparticles, where the introduced C=C groups on the surface of T-NdFeB microparticles are beneficial to increasing the cross-linking density within the T-NKP hydrogels. As the fractured chemically cross-linked PAm network is unable to be reformed, the self-healing behavior can only occur in the KC network through coil-helix transition and recombination of double helices with limited self-healing efficiency (38.2% for T-NKP-1.5 hydrogel, as shown in Fig. 2d, e), while the healed hydrogel can still withstand an elongation of about 70%. The recoverable and self-healing properties induced by heat treatment are sufficient for exploring magnetic hydrogels to bring interesting and potential applications.

The self-healing process is an essential fundamental to the modular assembly of magnetic hydrogels, while its magnetic property is crucial in determining the shape changes of hydrogels. The hysteresis loop of T-NKP-1.5 (Fig. 3a) shows its large coercivity (6800 Oe) with significant hard magnetism, which is the basis for the motion ability of magnetic soft robots under a magnetic field. A magnetically-induced bending deformation of end-fixed T-NKP hydrogel occurs when exposed to an external magnetic field perpendicular to its remanent magnetization (Fig. 3b). Under a fixed magnetic field of 18 mT, the bending angle of T-NKP hydrogel increases from 0° to 90° as the incorporated mass of T-NdFeB microparticles in the magnetic module increases from 0 to 2 g. T-NKP-1.5 and T-NKP-2 hydrogels exhibit maximum bending angles close to 90°, demonstrating their excellent magnetic responsiveness. As the poor mechanical property of the healed T-NKP-2 hydrogel

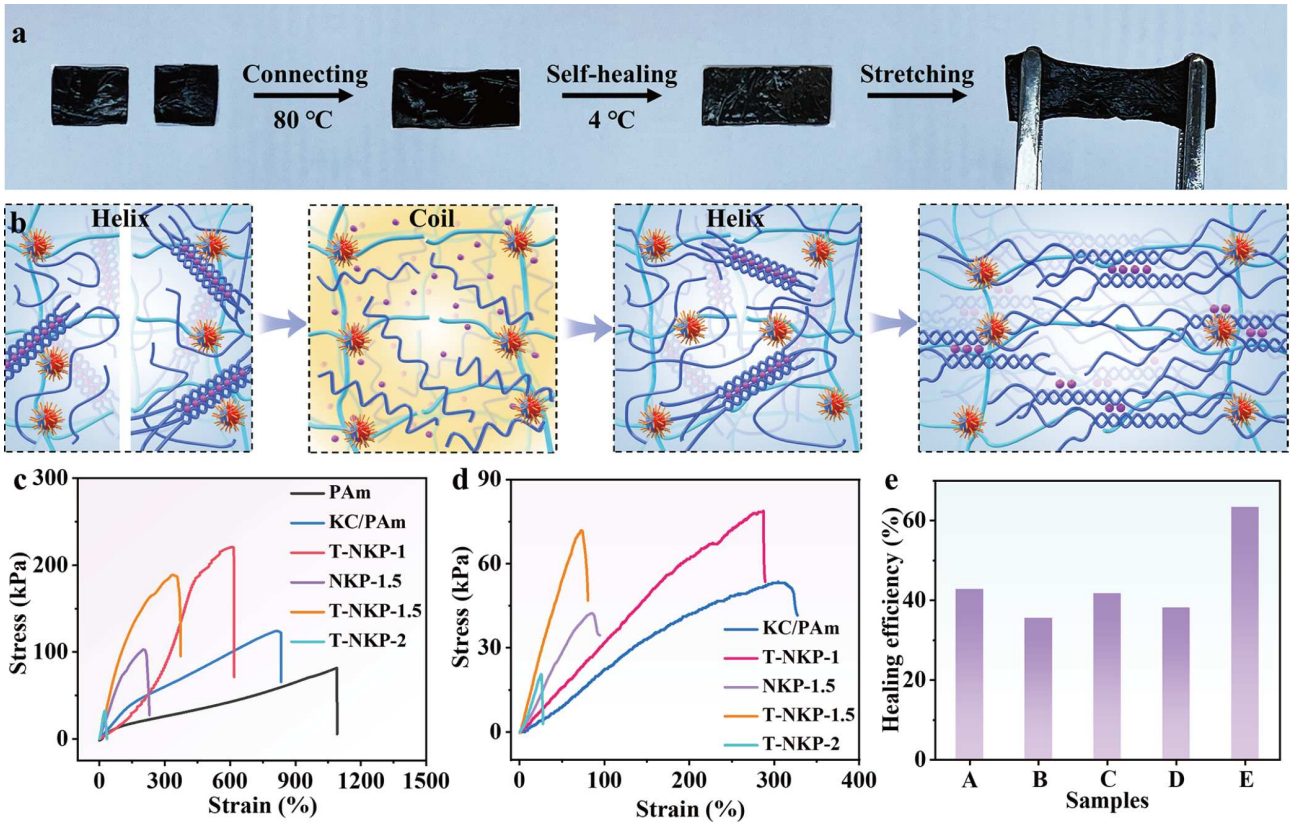

Figure 2 (a) Self-healing process of T-NKP hydrogel. (b) Schematic diagram of the self-healing process. Stress-strain curves of the (c) T-NKP and NKP hydrogels, and (d) self-healed T-NKP and NKP hydrogels. (e) Self-healing efficiency of T-NKP and NKP hydrogels, where A, B, C, D, and E represent KC/PAm, T-NKP-1, NKP-1.5, T-NKP-1.5, and T-NKP-2, respectively.

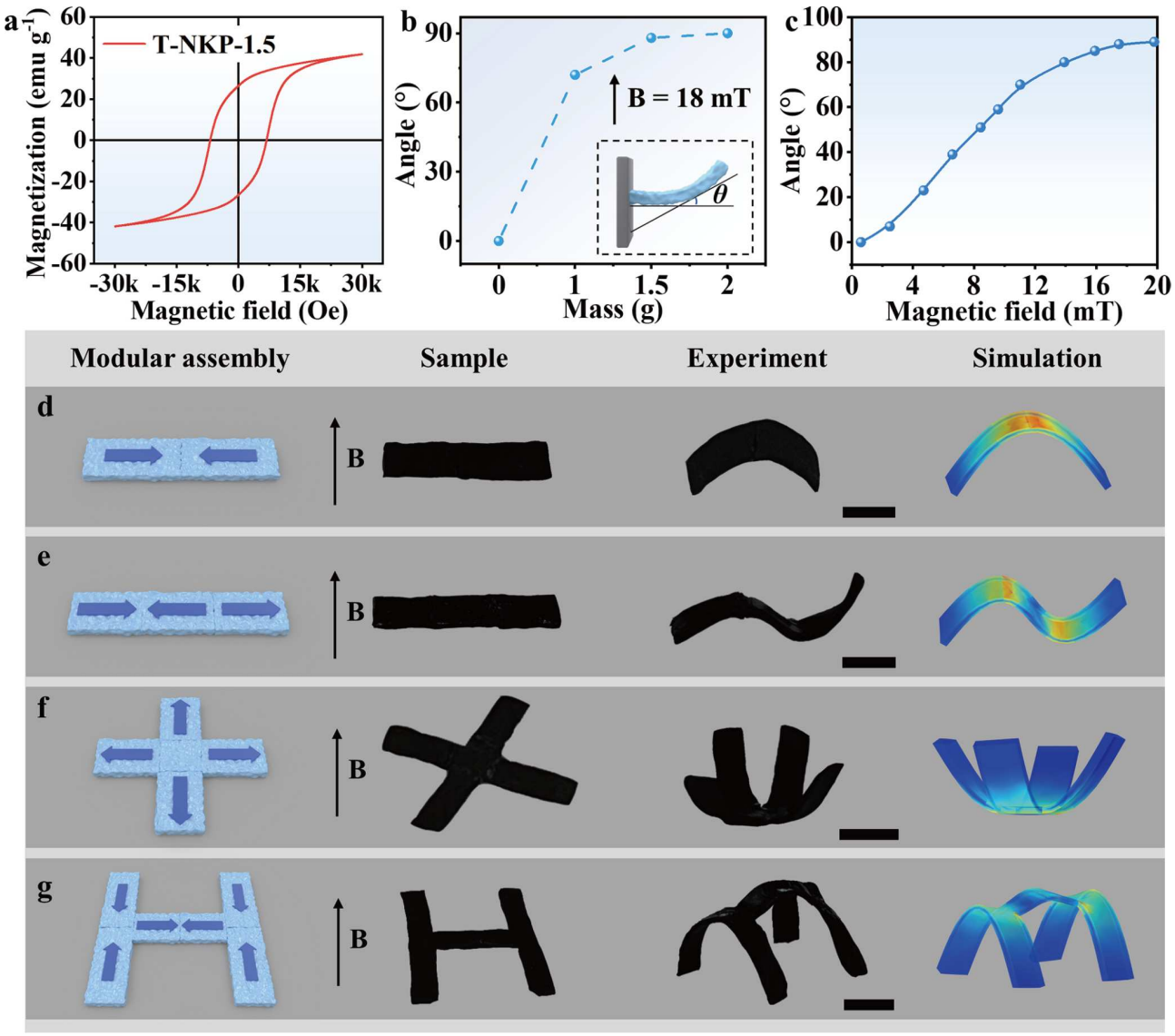

Figure 3 (a) Magnetization curve of T-NKP-1.5 hydrogel. (b) Bending angles of T-NKP hydrogel under a magnetic strength of 18 mT plotted against the mass of T-NdFeB in the T-NKP hydrogel. (c) Bending angle of T-NKP-1.5 hydrogel plotted against applied magnetic field strength from 0 to 20 mT. (d–g) Schematic designs, finite-element analysis, and experimental results of various assembled 2D planar structures (scale bar: 1 cm, B = 18 mT).

(Fig. 2d) is unfavorable for module assembly, the rectangular magnetized T-NKP-1.5 hydrogel is chosen as the magnetic module. As shown in Fig. 3c, the bending angle of the magnetic module increases from 0° to almost 90° with the increase of the magnetic field from 0 to 20 mT, which is favorable for controllable deformation of the magnetic modules by adjusting the magnetic field.

Furthermore, modular assemblies using different modules are efficient for the construction of stable 2D structures to satisfy the demands of different magnetization patterns and geometries. As shown in Fig. 3d–g, different shapes of magnetic soft robots are achieved through self-healing assembly of suitably sized magnetic modules, which are then deformed by an external magnetic field. The shape morphing of the assembled magnetic soft-robots (Fig. 3d–g) was also predicted by finite element analysis (FEA), which provides guidance for assembling other shapes of magnetic soft robots. Based on the experimentally measured mechanical and magnetic properties, the FEA simulation matches well with the experimental results. By taking the rectangular magnetic soft robot in Fig. 3d as an example, we observe that its two sides are subject to less stress under an applied magnetic field than that in the middle part, which is due to the opposite magnetization directions in these two magnetic modules. This modular assembly strategy can be used for further fabrication of complex 2D magnetization patterns to achieve complex shape morphing. In particular, the as-assembled "X"- and "H"-shaped models can even go through large deformations under an external magnetic field of 18 mT, as demonstrated by both experiments and FEA simulations in Fig. 3f, g.

The self-healing behavior of T-NKP-1.5 hydrogel allows not only the free combination of magnetic modules but also the integration of other functional modules, such as the ones containing photocatalysts for oxygen generation [41,42]. As a proof of concept, this study employs a Ru element doping strategy to design and develop a Ru-Bi_2CrO_6 photocatalyst with the aim of further enhancing its photocatalytic activity. As the X-ray dif-

fraction (XRD) patterns shown in Fig. 4a, the diffraction peaks of the Bi_2CrO_6 powder agree well with the simulated diffraction peaks obtained by triple-sloped phase Bi_2CrO_6, indicating that Bi_2CrO_6 was prepared successfully [18]. On the other hand, the XRD pattern of Ru-Bi_2CrO_6 displays negative deviation from that of Bi_2CrO_6, indicating that Ru doping does not affect the crystal structure of Bi_2CrO_6. The morphologies of Bi_2CrO_6 and Ru-Bi_2CrO_6 were investigated using transmission electron microscopy (TEM) and HAADF-STEM, as shown in Fig. 4b and Figs S6 and S7. Both Bi_2CrO_6 and Ru-Bi_2CrO_6 exhibit relatively regular plate-like morphologies with micrometer sizes. The EDS elemental mappings of Ru-Bi_2CrO_6 demonstrate the uniform distributions of Bi, Cr, O, and Ru elements, indicating the successful incorporation of Ru species onto the Bi_2CrO_6 (Fig. 4b). The high-resolution transmission electron microscopy (HRTEM) images (Fig. 4c, d) clearly show that the lattice spacing distances of Bi_2CrO_6 and Ru-Bi_2CrO_6 are 0.30 and 0.28 nm, respectively. This decrease in lattice spacing originates from the shrinkage of the Bi_2CrO_6 lattice after slight Ru doping. Additionally, X-ray photoelectron spectroscopy (XPS) was employed to reveal the electronic structures of Bi_2CrO_6 and Ru-Bi_2CrO_6. For Ru-Bi_2CrO_6, the two characteristic peaks of Ru 3p at 465.5 and 486.9 eV belong to Ru $3p_{3/2}$ and Ru $3p_{1/2}$, respectively, indicating that the valence state of Ru is close to +4 (Fig. S8) [43,44]. As shown in Fig. S9a (Supporting Information), the binding energy values of Bi appear at 158.7 and 164.0 eV in both Bi_2CrO_6 and Ru-Bi_2CrO_6, which are attributed to Bi^{3+} $4f_{7/2}$ and Bi^{3+} $4f_{5/2}$, respectively, indicating that the oxidation state of the Bi element remains essentially unchanged after doping of Ru [45]. In the case of Ru-Bi_2CrO_6, the Cr 2p XPS spectrum of Ru-Bi_2CrO_6 exhibits two new characteristic peaks at 586.4 and 576.4 eV corresponding to Cr^{3+} $2p_{1/2}$ and Cr^{3+} $2p_{3/2}$, respectively, alongside the characteristic peaks at 588.1 and 578.8 eV of Cr^{6+} (Fig. 4e). These observations suggest that the average valence state of Cr decreases upon Ru doping. Since the atomic radius of Ru is smaller than that of Bi, the Bi atoms in the main crystal are more easily replaced by Ru atoms [46,47]. This replacement of Bi^{3+} by Ru^{4+} with a higher valence necessitates a decrease in the average valence state of Cr to maintain charge equilibrium. The O 1s XPS spectra of Bi_2CrO_6 and Ru-Bi_2CrO_6 exhibit three characteristic peaks at binding energy values of 529.8, 531.6, and 533.4 eV (Fig. S9b), which are attributed to the lattice oxygen, adsorbed oxygen or hydroxyl groups, and surface-adsorbed H_2O, respectively [48–50]. To further analyze the coordination

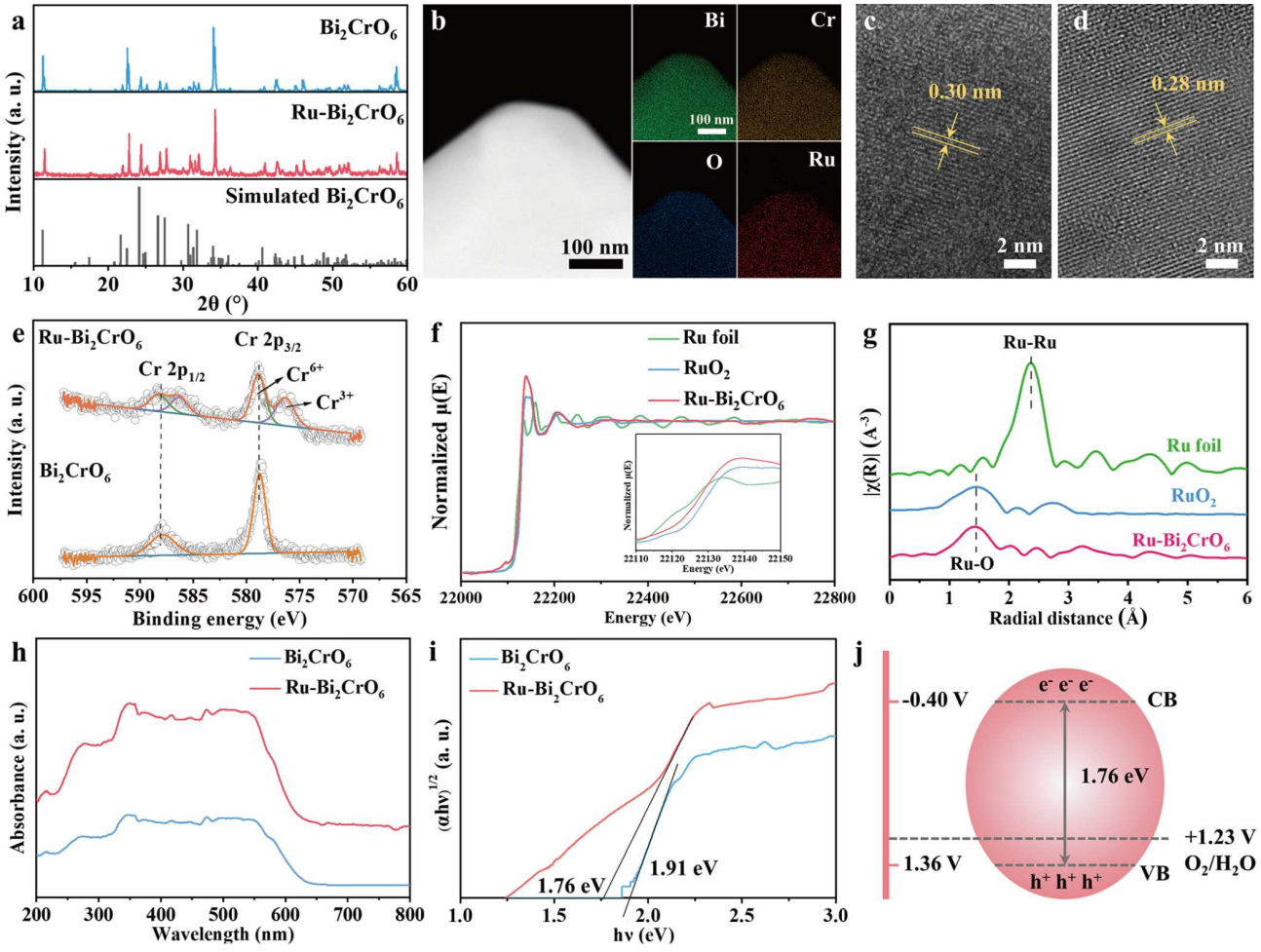

Figure 4 (a) XRD patterns of Bi_2CrO_6 and Ru-Bi_2CrO_6. (b) HAADF-STEM image and corresponding EDS elemental mappings of Ru-Bi_2CrO_6. HRTEM images of (c) Bi_2CrO_6 and (d) Ru-Bi_2CrO_6. (e) High-resolution XPS spectra of Cr 2p in Bi_2CrO_6 and Ru-Bi_2CrO_6. (f) Ru K-edge XANES profiles of Ru foil, RuO_2, and Ru-Bi_2CrO_6. The inset in (f) shows the magnified near-edge structures of different samples. (g) FT-EXAFS spectra of Ru K-edge for Ru foil, RuO_2, and Ru-Bi_2CrO_6. (h) UV-vis DRS spectra, and (i) band gap energy calculation (Tauc plot) of Bi_2CrO_6 and Ru-Bi_2CrO_6. (j) The diagram for the band structures of Ru-Bi_2CrO_6.

environment of Ru, X-ray absorption spectroscopy was employed. Fig. 4f exhibits the X-ray absorption near-edge spectrum (XANES) at Ru K-edge, confirming that the edge energy for Ru-Bi_2CrO_6 is lower than that of RuO_2, while higher than that of Ru foil, which suggests that Ru atoms in Ru-Bi_2CrO_6 carry positive charges $+\delta$ ($0 < \delta < 4$) [51]. The Fourier-transform extended X-ray absorption fine structure (FT-EXAFS) spectra for different samples indicate that Ru–O bonds are formed in Bi_2CrO_6 after Ru doping, with a bond length of 1.44 nm, and no Ru–Ru bonds are observed (Fig. 4g). To investigate the energy band structures of Bi_2CrO_6 and Ru-Bi_2CrO_6, ultraviolet-visible diffuse reflectance spectra (UV-Vis DRS) were recorded. As shown in Fig. 4h, the absorption threshold of Ru-Bi_2CrO_6 presents a red shift and indicates that the doped Ru element can broaden the absorption range of Bi_2CrO_6. On the basis of the Tauc curves by the Kubelka-Munk equation, the calculated band gap (E_g) values of Bi_2CrO_6 and Ru-Bi_2CrO_6 are 1.91 and 1.76 eV, respectively (Fig. 4i). The conduction band (CB) values of Bi_2CrO_6 and Ru-Bi_2CrO_6 were estimated according to Mott-Schottky curves. The slopes of the curves for both Bi_2CrO_6 and Ru-Bi_2CrO_6 are positive (Fig. S10), demonstrating that both of them are n-type semiconductors with flat band potentials (E_{FB} vs. Ag/AgCl) of −0.70 and −0.60 V, respectively. Therefore, the CB positions of Bi_2CrO_6 and Ru-Bi_2CrO_6 are estimated to be −0.50 and −0.40 V vs. NHE, respectively. According to the empirical formula ($E_g = E_{VB} - E_{CB}$), the valence band (VB) positions of Bi_2CrO_6 and Ru-Bi_2CrO_6 are 1.41 and 1.36 V vs. NHE (Fig. 4j and Table S1), respectively. The photoluminescence (PL) intensity of Ru-Bi_2CrO_6 is lower than that of Bi_2CrO_6 (Fig. S11), which indicates that the doped Ru can hinder the recombination of photo-generated carriers. Furthermore, the electrochemical performance of the Bi_2CrO_6 and Ru-Bi_2CrO_6 was studied by transient photocurrent and electrochemical impedance spectra (EIS) to provide information on their charge separation and transfer dynamics [52]. As shown in Fig. S12, the photocurrent density of Ru-Bi_2CrO_6 reaches 1.36 times that of pristine Bi_2CrO_6, demonstrating that Ru doping substantially improves the separation and transport efficiency of charge carriers. The charge transfer resistance was calculated according to the Nyquist plots [53]. After Ru doping, the resistance decreases from 64.3 to 48.3 kΩ (Fig. S13), leading to an increased charge separation efficiency of Ru-Bi_2CrO_6 with enhanced carrier transfer dynamics at the interface between photocatalyst and solution.

Based on previously discussed band structures of Bi_2CrO_6 and Ru-Bi_2CrO_6, their oxygen generation efficiencies were systematically examined with the objective of thoroughly assessing their capability in boosting the DO concentrations within aquatic surroundings. The oxygen content generated was quantitatively assessed via gas chromatography, with the corresponding standard curve shown in Fig. S14. As illustrated in Fig. 5a, stable and efficient photocatalysis can be achieved by Bi_2CrO_6 with an O_2 yield of 148.4 μmol g^{-1} h^{-1}, while the efficiency of photocatalytic water oxidation is further improved after doping with a Ru atom (O_2 yield: 391.9 μmol g^{-1} h^{-1}). The produced O_2 amount of Ru-Bi_2CrO_6 is almost 1.6 times higher than that of Bi_2CrO_6 after 3 h (Fig. S15), demonstrating the positive role of doped Ru atoms in enhancing the photocatalytic oxygen evolution of Ru-Bi_2CrO_6. The results in Table S2 (Supporting Information) indicate that Ru-Bi_2CrO_6 demonstrates superior oxygen generation efficiency compared to most of the reported photocatalysts. The XRD pattern of Ru-Bi_2CrO_6 after photocatalysis is consistent with its original pattern, affirming the unaltered integrity of its crystalline lattice and its excellent structural stability (Fig. S16). Furthermore, the Ru-Bi_2CrO_6 photocatalyst maintains 88.2% of its initial activity after five successive cycles (Fig. S17), indicating its exceptional recyclability. The slight decline in performance during recyclability testing is mainly attributed to the reduction in the number of active sites from the joint effects of photocorrosion and catalyst agglomeration [54,55]. Additionally, density functional theory (DFT) calculations were carried out to investigate the structure-property relationship between Ru-Bi_2CrO_6 and its enhanced water oxidation performance. According to the charge density differences (Fig. 5b, c), the Bi_2CrO_6 model acquires only 0.013 electron during water adsorption, whereas the Ru-Bi_2CrO_6 model gains an additional 0.024 electron, indicating Ru-induced electronic redistribution facilitates stronger interfacial water chemisorption. This optimized charge environment promotes subsequent oxygen evolution kinetics through improved reactant activation. The catalytic sites on Bi_2CrO_6 and Ru-Bi_2CrO_6 models were investigated by tracking the consecutive electron transfer steps during the water oxidation process. The schematic diagrams for oxygen generation steps on both Bi_2CrO_6 and Ru-Bi_2CrO_6 models are presented in Fig. 5d, with corresponding Gibbs free energy (ΔG) values depicted in Table S3 (Supporting Information). The oxygen generation process proceeds via a four-electron transfer pathway with three transient intermediates, involving *OH, *O, and *OOH [56]. As revealed by DFT calculations, the Bi atom in the Bi_2CrO_6 model is the active site for photocatalytic oxygen generation, showing the highest potential barrier (ΔG = 2.05 eV) on deprotonation of $*H_2O$ species to generate *OH species, which is regarded as the potential-determining step. For the Ru-Bi_2CrO_6 model, the Bi atom serves as the active site. The highest potential barrier during the deprotonation of $*H_2O$ to *OH drops to 1.91 eV, indicating enhanced intrinsic activity for oxygen generation.

Subsequently, the Ru-Bi_2CrO_6 photocatalyst was incorporated into the KC/PAm hydrogel to obtain the functional module (photocatalytic module) for oxygen generation, which was further assembled with the magnetic actuation module and resulted in the fabrication of OGR. The mechanical properties of the photocatalytic module (Ru-Bi_2CrO_6/KC/PAm), the healed Ru-Bi_2CrO_6/KC/PAm, and OGR were evaluated (Fig. S18). The results show that the self-healing efficiency of the photocatalytic module is 42.3%, which is comparable to that of KC/PAm (42.9%). This is primarily attributed to the fact that the self-healing property is predominantly governed by KC within the composite hydrogel. Fig. S18 also indicates that the OGR assembled via the self-healing process of the KC/PAm hydrogel matrix can withstand a maximum stress of 51.6 kPa, demonstrating the excellent stability of the assembled OGR, which is crucial for the effective actuation of the OGR under a realistic environment. Based on these results, the OGR was designed and fabricated into the shape shown in Fig. 5e, with its tail's magnetic actuation module programmed with magnetization to facilitate directed motion under an external magnetic field. The tail of the robot oscillates by changing the direction of the external magnetic field in the Z-direction, which, in turn, generates a propulsion force and makes the robot move forward. By adjusting the magnetic fields in the X- and Y-directions, the motion direction of the OGR can be precisely controlled,

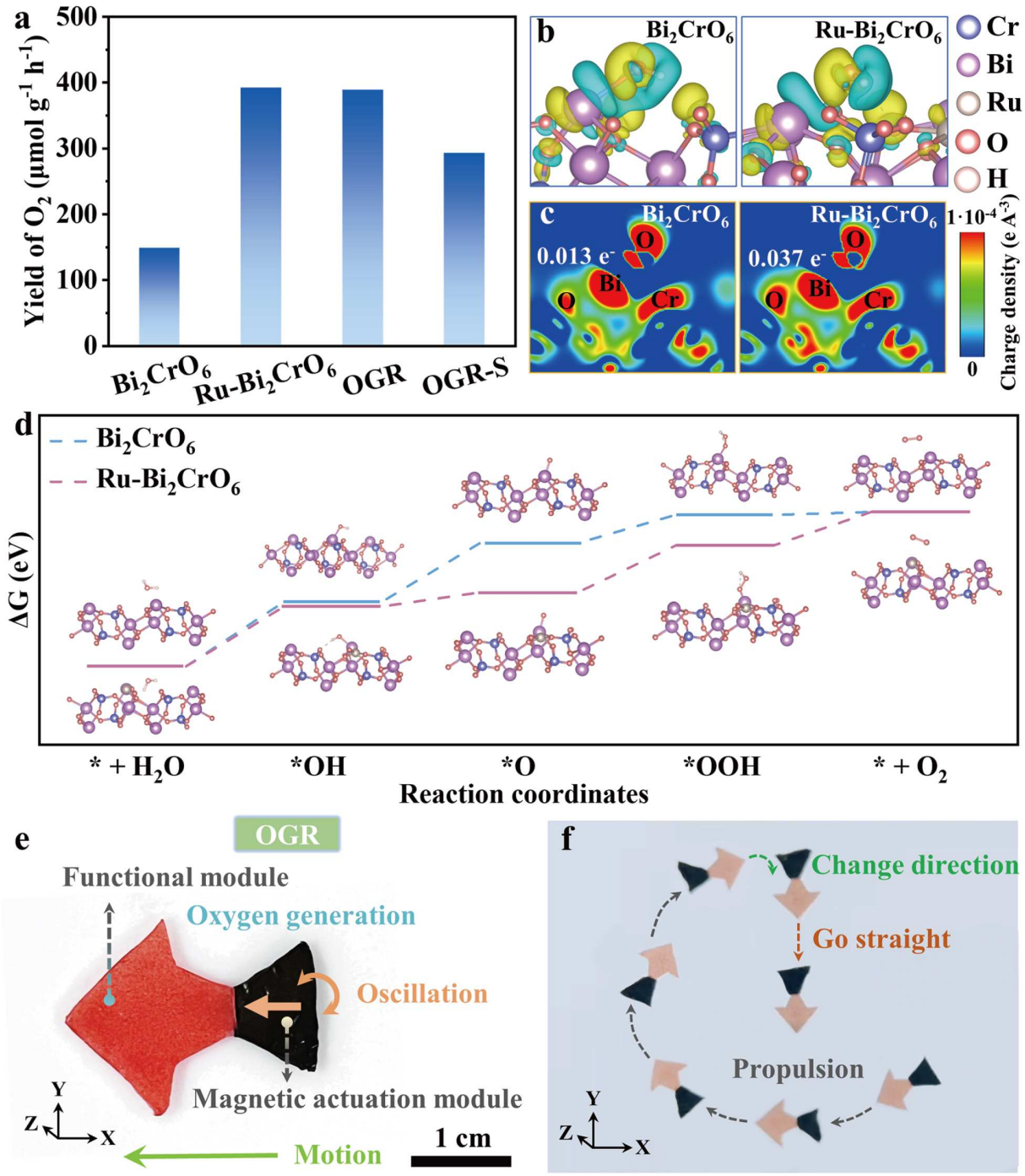

Figure 5 (a) Photocatalytic oxygen generation performance of Bi_2CrO_6, Ru-Bi_2CrO_6, OGR under actuation, and OGR-S. (b) Charge density differences and (c) corresponding 2D contour maps of Bi_2CrO_6 and Ru-Bi_2CrO_6. The yellow and cyan areas represent the accumulation and depletion of electrons, respectively. (d) Gibbs free energy values for the photocatalytic oxygen generation processes on Bi_2CrO_6 and Ru-Bi_2CrO_6 models. (e) Photograph and working principle of OGR. (f) Complex motion trajectory of OGR.

enabling it to quickly steer. As a result, the OGR can accurately navigate to the target area through the aforementioned process (Fig. 5e, f and Movie S1). Specifically, Fig. 5a shows that the oxygen generation rate of the OGR under stationary conditions (OGR-S, "S" represents the stationary state) reaches 292.8 μmol g^{-1} h^{-1}, significantly lower than that under actuation. This enhancement is primarily due to the dynamic behavior, which facilitates the desorption of products from the catalyst surface, thereby accelerating the oxygen generation efficiency. This clearly highlights the significant improvement of the photocatalytic process by the actuatable soft robot. The oxygen generation rate of OGR (389.1 μmol g^{-1} h^{-1}) under actuation is comparable to that of Ru-Bi_2CrO_6 powder, underscoring that the OGR can fully harness its photocatalytic potential without the requirement of supplementary energy input (e.g., mechanical agitation). To further explore the practical implications and effectiveness of OGR in real-world aquatic scenarios, the DO concentrations in water before and after

catalysis at multiple positions were measured. At an ambient temperature of 20 °C, the initial DO concentration was recorded to be 9.0 mg L^{-1}. Subsequently, a hypoxic water environment was successfully simulated by bubbling Ar gas for 30 min, where the DO concentration reduced to 6.4 mg L^{-1}. Following this, five OGRs were placed in this simulated environment, and their photocatalytic oxygen generation reactions were confined to a localized area. After 6 h of illumination, spatially resolved measurements of the DO concentration were taken in the water. As shown in Fig. S19a, the DO concentration near the OGR increases significantly to 9.4 mg L^{-1}. As the distance from the OGR increases, however, the DO concentration decreases gradually, with a concentration of 7.6 mg L^{-1} measured at a distance of 30 cm from the OGR. These findings demonstrate that the OGR can effectively enhance the DO concentration in localized water areas and create a distinct oxygen concentration gradient, thereby providing direct evidence for improving oxygen supply in target aquatic environments. These results not only demonstrate the remarkable flexibility of the OGR but also highlight its capacity to efficiently deliver oxygen to the target area (Fig. S19b), further confirming the feasibility of OGR in practical applications.

CONCLUSIONS

In conclusion, a magnetically actuated soft robot has been successfully developed by integrating functionalized magnetic microparticles (T-NdFeB) into a KC/PAm double-network hydrogel matrix. The unique properties of this hydrogel, including self-healing behavior and magnetic actuation, enable the free assembly of these magnetic actuation modules to achieve multiple morphing, with the deformation results closely matching the shapes predicted by FEA simulation. Furthermore, an efficient photocatalyst for oxygen generation (391.9 μmol g^{-1} h^{-1}) was developed by doping Ru into Bi_2CrO_6. The reaction mechanism of photocatalytic oxygen generation was also analyzed by DFT calculations, revealing that Ru doping significantly reduces the energy barrier during the oxygen generation reaction. As a proof of concept, functional modules were produced by incorporating the Ru-Bi_2CrO_6 component into the KC/PAm hydrogel. These functional modules were subsequently assembled with a magnetic actuation module to obtain a flexible OGR. The OGR demonstrates excellent maneuverability and targeted oxygen delivery capabilities (389.1 μmol g^{-1} h^{-1}), making it a promising candidate for enhancing oxygen content in aquatic environments and other relevant applications. This study provides a new paradigm for designing programmable soft robots and the convenient integration of functionalities.

Received 19 May 2025; accepted 8 July 2025; published online 29 October 2025

1 Park CS, Kang YW, Na H, *et al.* Hydrogels for bioinspired soft robots. Prog Polym Sci, 2024, 150: 101791
2 Yao DR, Kim I, Yin S, *et al.* Multimodal soft robotic actuation and locomotion. Adv Mater, 2024, 36: 2308829
3 Yang Z, Xu C, Lee JX, *et al.* Magnetic miniature soft robot with reprogrammable drug-dispensing functionalities: toward advanced targeted combination therapy. Adv Mater, 2024, 36: 2408750
4 Qin J, Li J, Chu K, *et al.* Biomimetic solar photocatalytic reactor for selective oxidation of aromatic alcohols with enhanced solar-energy utilization. Adv Funct Mater, 2024, 34: 2311214
5 Zhou H, Mayorga-Martinez CC, Pané S, *et al.* Magnetically driven micro and nanorobots. Chem Rev, 2021, 121: 4999–5041
6 Liu D, Xiao Y, Yang KK, *et al.* From dynamic molecular bridging to achieving Healable, recyclable, photo/magnetic-responsive shape memory EVA@Fe_3O_4 hybrid network. Compos Commun, 2024, 49: 101959
7 Zhu G, Hou Y, Xia N, *et al.* Fully recyclable, healable, soft, and stretchable dynamic polymers for magnetic soft robots. Adv Funct Mater, 2023, 33: 2300888
8 Podstawczyk D, Nizioł M, Szymczyk P, *et al.* 3D printed stimuli-responsive magnetic nanoparticle embedded alginate-methylcellulose hydrogel actuators. Additive Manufacturing, 2020, 34: 101275
9 Kim Y, Zhao X. Magnetic soft materials and robots. Chem Rev, 2022, 122: 5317–5364
10 Deng C, Qu J, Dong J, *et al.* 4D printing of magnetic smart structures based on light-cured magnetic hydrogel. Chem Eng J, 2024, 494: 152992
11 Ganguly S, Margel S. 3D printed magnetic polymer composite hydrogels for hyperthermia and magnetic field driven structural manipulation. Prog Polym Sci, 2022, 131: 101574
12 Qin J, Li J, Yang G, *et al.* A bio-inspired magnetic soft robotic fish for efficient solar-energy driven water purification. Small Methods, 2025, 9: 2400880
13 Fang Y, Hou Y, Fu X, *et al.* Semiconducting polymers for oxygen evolution reaction under light illumination. Chem Rev, 2022, 122: 4204–4256
14 Liu Y, Wang LJ, Zhang H, *et al.* Boosting photocatalytic water oxidation over bifunctional Rh^0-Rh^{3+} sites. Angew Chem Int Ed, 2021, 60: 22761–22768
15 Shen R, Qin C, Hao L, *et al.* Realizing photocatalytic overall water splitting by modulating the thickness-induced reaction energy barrier of fluorenone-based covalent organic frameworks. Adv Mater, 2023, 35: 2305397
16 Chen X, Xu Y, Ma X, *et al.* Large dipole moment induced efficient bismuth chromate photocatalysts for wide-spectrum driven water oxidation and complete mineralization of pollutants. Natl Sci Rev, 2020, 7: 652–659
17 Liao WX, Zhao XL, Wang TS. A $Bi_{7.38}Cr_{0.62}O_{12+x}$ crystal as a novel visible-light-active photocatalyst up to ~650 nm. RSC Adv, 2017, 7: 28797–28801
18 Tao X, Zhou H, Zhang C, *et al.* Triclinic-phase bismuth chromate: a promising candidate for photocatalytic water splitting with broad spectrum ranges. Adv Mater, 2023, 35: 2211182
19 Chen Z, Fang Y, Wang L, *et al.* Remarkable oxygen evolution by Co-doped ZnO nanorods and visible light. Appl Catal B-Environ, 2021, 296: 120369
20 Lin S, Huang H, Ma T, *et al.* Photocatalytic oxygen evolution from water splitting. Adv Sci, 2021, 8: 2002458
21 Gao H, Zhu L, Zhang G, *et al.* Defects-rich Ru-doped black TiO_2 nanotube arrays for photoelectrochemical levofloxacin degradation coupled with simultaneous cathodic H_2 production. J Colloid Interface Sci, 2025, 688: 677–687
22 Tang J, Su C, Shao Z. Advanced membrane-based electrode engineering toward efficient and durable water electrolysis and cost-effective seawater electrolysis in membrane electrolyzers. Exploration, 2024, 4: 20220112
23 Chen K, Xiao J, Vequizo JJM, *et al.* Overall water splitting by a $SrTaO_2N$-based photocatalyst decorated with an Ir-promoted Ru-based cocatalyst. J Am Chem Soc, 2023, 145: 3839–3843
24 Cao W, Zhang W, Dong L, *et al.* Progress on quantum dot photocatalysts for biomass valorization. Exploration, 2023, 3: 20220169
25 Kuang X, Wu S, Ze Q, *et al.* Magnetic dynamic polymers for modular assembling and reconfigurable morphing architectures. Adv Mater, 2021, 33: 2102113
26 Deng H, Sattari K, Xie Y, *et al.* Laser reprogramming magnetic anisotropy in soft composites for reconfigurable 3D shaping. Nat Commun, 2020, 11: 6325
27 Kim Y, Yuk H, Zhao R, *et al.* Printing ferromagnetic domains for untethered fast-transforming soft materials. Nature, 2018, 558: 274–279
28 Gu H, Boehler Q, Ahmed D, *et al.* Magnetic quadrupole assemblies with arbitrary shapes and magnetizations. Sci Robot, 2019, 4: eaax8977

29 Xu M, Liao J, Li J, *et al.* Elastic nanoparticle-reinforced, conductive structural color hydrogel with super stretchability, self-adhesion, self-healing as electrical/optical dual-responsive visual electronic skins. Exploration, 2025, 5: 270008
30 Guo Y, Bae J, Fang Z, *et al.* Hydrogels and hydrogel-derived materials for energy and water sustainability. Chem Rev, 2020, 120: 7642–7707
31 Khadka A, Pradhan S, Samuel E, *et al.* Rapidly self-healing, highly conductive, stretchable, body-attachable hydrogel sensor for soft electronics. Compos Commun, 2024, 52: 102158
32 Nie L, Ding X, Lin Y, *et al.* Self-healing, adhesive, antibacterial, and biocompatible hydrogel dressings using sialic acid substituted chitosan and oxidized pullulan with incorporation of epigallocatechin gallate. Compos Commun, 2024, 51: 102107
33 Xia X, Cao X, Zhang B, *et al.* Human skin-mimicking ionogel-based electronic skin for intelligent robotic sorting. Macromol Rapid Commun, 2025, 46: 2400379
34 Tan X, Chu K, Chen Z, *et al.* Recent advances in self-healing hydrogel composites for flexible wearable electronic devices. Nano Res Energy, 2024, 3: e9120123
35 Miao Y, Xu M, Zhang L. Electrochemistry-induced improvements of mechanical strength, self-healing, and interfacial adhesion of hydrogels. Adv Mater, 2021, 33: 2102308
36 Liu S, Li L. Ultrastretchable and self-healing double-network hydrogel for 3D printing and strain sensor. ACS Appl Mater Interfaces, 2017, 9: 26429–26437
37 Liu S, Li L. Recoverable and self-healing double network hydrogel based on κ-carrageenan. ACS Appl Mater Interfaces, 2016, 8: 29749–29758
38 Wang L, Huang T, Xu X, *et al.* Robust dual equivariant gradient antibacterial wound dressing-loaded artificial skin with nano-chitin particles via an electrospinning-reactive strategy. Adv Fiber Mater, 2025, 7: 204–218
39 Chen Z, Shen T, Zhang M, *et al.* Tough, anti-fatigue, self-adhesive, and anti-freezing hydrogel electrolytes for dendrite-free flexible zinc ion batteries and strain sensors. Adv Funct Mater, 2024, 34: 2314864
40 Zhou L, Zhang W, Zhao C, *et al.* Self-cross-linkable maleic anhydride terpolymer coating with inherent high antimicrobial activity and low cytotoxicity. ACS Appl Mater Interfaces, 2023, 15: 47810–47821
41 Cheng J, Cheng B, Xu J, *et al.* Organic-inorganic S-scheme heterojunction photocatalysts: design, synthesis, applications, and challenges. eScience, 2025, 5: 100354
42 Ding Y, Yang G, Xiang Z, *et al.* Design of two-dimensional porous photocatalysts and their applications in solar fuel and valuable chemical production. J Environ Chem Eng, 2024, 12: 113483
43 Fan L, Shen H, Ji D, *et al.* Biaxially compressive strain in Ni/Ru core/shell nanoplates boosts Li–CO_2 batteries. Adv Mater, 2022, 34: 2204134
44 Xu G, Zhang Y, Fu Y, *et al.* Efficient hydrogenation of various renewable oils over Ru-HAP catalyst in water. ACS Catal, 2017, 7: 1158–1169
45 Sun Z, Yang X, Yu XF, *et al.* Surface oxygen vacancies of Pd/Bi_2MoO_{6-x} acts as "Electron Bridge" to promote photocatalytic selective oxidation of alcohol. Appl Catal B-Environ, 2021, 285: 119790
46 Wang B, Zeng Y, Xiong M, *et al.* Adsorption performance and mechanism of mesoporous carbon-doped Al_2O_3 adsorbent derived from NH_2-MIL-53 (Al) for removing Cr(VI) and methyl orange from aqueous solution. J Environ Chem Eng, 2023, 11: 110081
47 Chen F, Wu X, Shi C, *et al.* Molecular engineering toward pyrrolic N-rich M–N_4 (M = Cr, Mn, Fe, Co, Cu) single-atom sites for enhanced heterogeneous fenton-like reaction. Adv Funct Mater, 2021, 31: 2007877
48 Guo H, Zhou Y, Chu K, *et al.* Improved ammonia synthesis and energy output from zinc-nitrate batteries by spin-state regulation in perovskite oxides. J Am Chem Soc, 2025, 147: 3119–3128
49 Chu K, Zong W, Xue G, *et al.* Cation substitution strategy for developing perovskite oxide with rich oxygen vacancy-mediated charge redistribution enables highly efficient nitrate electroreduction to ammonia. J Am Chem Soc, 2023, 145: 21387–21396
50 Liu L, Dong H, Huang S, *et al.* Charge-redistribution in bimetallic oxides buried in microporous curled carbon for efficient nitrate electroreduction to ammonia. Sci China Mater, 2025, 68: 472–482
51 Guo H, Guo Z, Xue G, *et al.* Entropy-driven stabilization of noble metal single atoms: advancing ammonia synthesis and energy output in zinc-nitrate batteries. Adv Mater, 2025, 37: 2500224
52 Long Z, Zheng X, Shi H. Construction of $BiVO_4$/CoPc S-scheme heterojunctions with enhanced photothermal-assisted photocatalytic activity. Sci China Mater, 2024, 67: 550–561
53 Gao X, An L, Qu D, *et al.* Enhanced photocatalytic N_2 fixation by promoting N_2 adsorption with a co-catalyst. Sci Bull, 2019, 64: 918–925
54 Martín AJ, Mitchell S, Mondelli C, *et al.* Unifying views on catalyst deactivation. Nat Catal, 2022, 5: 854–866
55 Meißner A, Alberico E, Drexler HJ, *et al.* Rhodium diphosphine complexes: a case study for catalyst activation and deactivation. Catal Sci Technol, 2014, 4: 3409–3425
56 He F, Wang S, Lu Y, *et al.* Unification of hot spots and catalytic sites on isolated boron centers in porous carbon nitride nanosheets for efficient photocatalytic oxygen evolution. Nano Energy, 2023, 116: 108800

Acknowledgement This work was financially supported by the National Natural Science Foundation of China (52303151), the Fundamental Research Funds for the Central Universities (YG2025QNA05), the National Key Research and Development Program of China (2022YFB3805700), the Research Foundation Flanders (1298323N), the Program of the Shanghai Academic Research Leader (17XD1400100), the Shanghai Key Laboratory of Material Frontiers Research in Extreme Environments (MFree) of China (22dz2260800), and the Shanghai Science and Technology Committee of China (22JC1410300). This work was supported by the BL17B station of the National Facility for Protein Science in Shanghai (NFPS) and the BL13SSW station at Shanghai Synchrotron Radiation Facility (SSRF) in characterizations. The characterizations were also carried out with the support of the Central Laboratory, School of Chemical and Material Engineering, Jiangnan University. The numerical calculations have been done on the supercomputing system in Hefei Advanced Computing Center and the Supercomputing Center of the University of Science and Technology of China.

Author contributions Qin J and Chu K designed and engineered the samples; Qin J, Li J, Chen H, Xuan P, Wu X, and Dong H performed the experiments; Peng X, Qian Y, Chen Y, Fan W, and Liu T conceived the post-fabrication tuning of random modes; Qin J, Li J, and Lai F wrote the paper with support from Osella S. All authors contributed to the general discussion.

Conflict of interest The authors declare that they have no conflict of interest.

Supplementary information Supplementary materials are available in the online version of the paper.

Jingjing Qin received her BE degree from Qingdao Agricultural University. She is currently a PhD student at Jiangnan University. Her research focuses on the design of light/magnetic-driven soft robots and their integration with functionalities such as photocatalysis and water treatment applications.

Feili Lai earned his BS degree from Donghua University (2014), MS degree from Fudan University (2017), and his PhD degree from the Max Planck Institute of Colloids and Interfaces/Universität Potsdam (2019). He is currently an associate professor at the School of Materials Science and Engineering, Shanghai Jiao Tong University. His research interests include the design and synthesis of low-dimensional solids and composites for energy storage and conversion applications.

基于自愈合水凝胶模块化组装策略的磁性产氧机器人

秦静静[1†], 李嘉豪[2†], 楚凯斌[1], 陈昊祥[3], 宣鹏洋[1], 吴秀明[1], 董洪亮[4,7], 彭咲远[5], 钱运[5], Silvio Osella[6], 陈玉洁[3], 樊玮[1], 刘天西[1], 赖飞立[3,8*]

摘要 磁性水凝胶机器人因具备远程可控性、灵活性、生物相容性及化学稳定性等优势, 在生物医学及水下环境中极具应用前景, 但功能单一性制约了其进一步发展. 本研究提出一种模块化组装策略: 通过将磁性颗粒嵌入κ-卡拉胶/聚丙烯酰胺水凝胶中获得磁驱动模块, 利用其自愈合能力实现磁驱动模块的自由组装, 从而构建可编程水凝胶机器人. 该机器人在磁场下可执行多种形变行为. 此外, 该策略支持功能性集成.例如, 将磁驱动模块与负载Ru-Bi_2CrO_6光催化剂的功能模块组合, 构建出兼具运动与产氧功能的软机器人. 该机器人通过磁控振荡行为在水下实现低扰动运动, 产氧速率达389.1 μmol g^{-1} h^{-1}, 可为特定水域持续供氧. 产氧机器人的水凝胶骨架不仅能有效抑制光催化颗粒的团聚和沉降, 还可便捷地利用磁场进行回收. 本研究为软机器人的设计和多功能集成提供了一种便捷且适应性强的方法.